

Cheap2Rich: A Multi-Fidelity Framework for Data Assimilation and System Identification of Multiscale Physics - Rotating Detonation Engines

Yuxuan Bao ^{*1} Jan Zajac ^{*23} Megan Powers ⁴ Venkat Raman ⁴ J. Nathan Kutz ^{1,2}

Abstract

Bridging the sim2real gap between computationally inexpensive models and complex physical systems remains a central challenge in machine learning applications to engineering problems, particularly in multi-scale settings where reduced-order models typically capture only dominant dynamics. In this work, we present Cheap2Rich, a multi-scale data assimilation framework that reconstructs high-fidelity state spaces from sparse sensor histories by combining a fast low-fidelity prior with learned, interpretable discrepancy corrections. We demonstrate the performance on rotating detonation engines (RDEs), a challenging class of systems that couple detonation-front propagation with injector-driven unsteadiness, mixing, and stiff chemistry across disparate scales. Our approach successfully reconstructs high-fidelity RDE states from sparse measurements while isolating physically meaningful discrepancy dynamics associated with injector-driven effects. The results highlight a general multi-fidelity framework for data assimilation and system identification in complex multi-scale systems, enabling rapid design exploration and real-time monitoring and control while providing interpretable discrepancy dynamics. Code for this project is available at: github.com/kro011k/Cheap2Rich.

1. Introduction

Despite significant advancements in physics-informed AI (Kutz et al., 2025; Karniadakis et al., 2021; Brunton & Kutz, 2022; Wyder et al., 2025; Fan et al., 2025) and

^{*}Equal contribution ¹Department of Applied Mathematics, University of Washington, Seattle, USA ²Department of Electrical and Computer Engineering, University of Washington, Seattle, USA ³Department of Mathematics, Swiss Federal Institute of Technology Zurich, Zurich, Switzerland ⁴University of Michigan, Advanced Propulsion Concepts Lab, Ann Arbor, USA. Correspondence to: J. Nathan Kutz <kutz@uw.edu>.

Preprint. January 29, 2026.

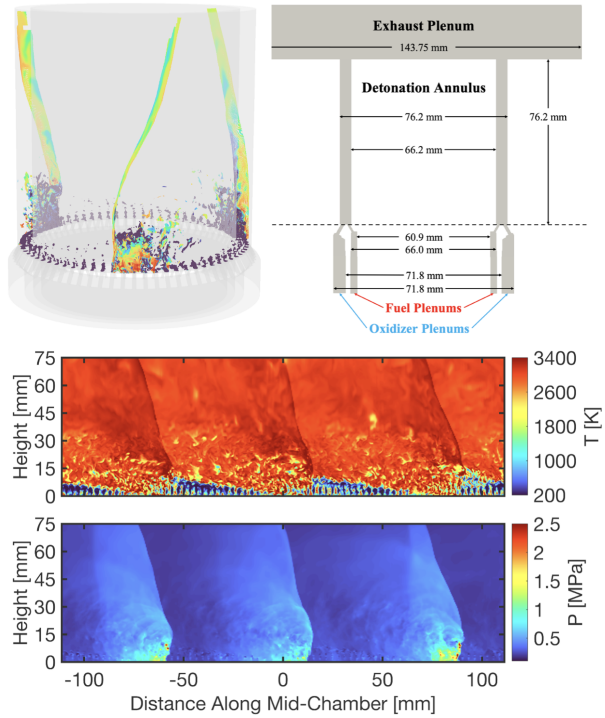


Figure 1. A rotating detonation rocket engine (RDRE). Full-scale geometry (top left) and cross-sectional schematic with primary dimensions (top right) Temperature and Pressure mid-channel contour projections (bottom).

neural operators (Lu et al., 2021; Li et al., 2020; Roy et al., 2025), modeling of multi-scale physics remains a grand challenge due to the inability of methods to model the orders of magnitude different time and space scales present in complex systems. Traditional machine learning methods typically capture the dominant large scale time and space features due to the spectral bias in training (Rahaman et al., 2019). Thus important characteristics and features are effectively band-pass filtered in model training. We introduce a neural network architecture that by construction targets different scales for training. Specifically, Data assimilation (DA) (Ghil & Malanotte-Rizzoli, 1991; Bocquet et al., 2019) provides a principled framework for closing the performance gap in multiscale modeling by combining physics-based prediction and experimental observation.

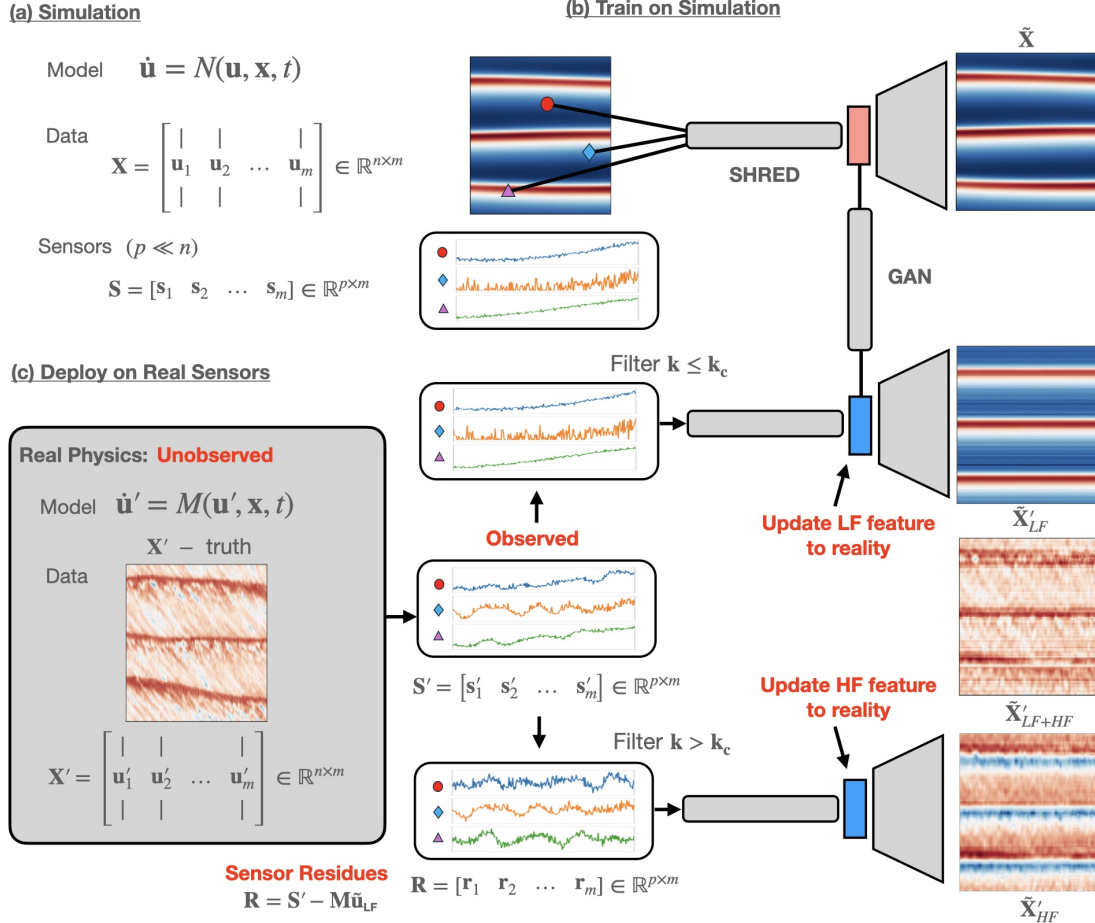


Figure 2. The Cheap2Rich architecture. (a) Simulation model provides full-state data \mathbf{X} and sparse sensor measurements \mathbf{S} . (b) A standard SHRED network is trained on simulation data to reconstruct full states $\tilde{\mathbf{X}}$ from sensor histories. (c) Deployment on real sensors: the real physics full state \mathbf{X}' is unobserved; only sparse sensor measurements \mathbf{S}' are available. The LF DA-SHRED pathway updates the latent features to reality, producing $\tilde{\mathbf{X}}'_{LF}$. The HF pathway processes sensor residuals \mathbf{R} to capture fine-scale corrections $\tilde{\mathbf{X}}'_{HF}$. The final reconstruction $\tilde{\mathbf{X}}'_{LF+HF}$ combines both pathways to close the simulation-to-reality gap.

Recent advances in latent dynamical system learning (Erichson et al., 2020; Jiang et al., 2025), including the Shallow Recurrent Decoder (SHRED) framework (Williams et al., 2024; Tomasetto et al., 2025; Bao & Kutz, 2025), further enable the discovery of compact latent representations and missing functional structure directly from data. However, the application of DA-enhanced latent learning to strongly nonlinear, multistable systems with sparse, noisy measurements remains largely unexplored (Niu et al., 2024; Liu et al., 2024).

In this work, we introduce a multi-scale data assimilation pipeline that bridges a fast reduced-order RDE model and high-fidelity dynamics using only sparse sensor histories. The method augments a SHRED framework trained on multiscale data with a deployment-time assimilation mechanism that separates the reconstruction into (i) a low-frequency (LF) component, aligned to the sensor-induced latent distri-

bution via a lightweight latent-GAN and explicitly low-pass filtered, and (ii) a high-frequency (HF) correction learned directly from sensor-space residuals and regularized to be spectrally sparse. This decomposition enforces a clean division between dominant features that the reduced model already captures and fine-scale discrepancies induced by unmodeled or unresolved physics, yielding a unified surrogate that is both accurate and diagnostically informative.

Rotating detonation engines (RDEs), which are an ideal test case for our method due to the inherent multiscale physics, offer a promising pathway toward high-efficiency propulsion and power generation by sustaining continuous detonation waves within an annular combustor (Sato et al., 2021; 2025; Nakagami et al., 2017; Wolański, 2013). However, the underlying physics of RDEs is governed by tightly coupled compressible flow, shock-detonation interactions, stiff chemical kinetics, and injector-driven mass, momentum,

and energy exchange across disparate spatial and temporal scales (Raman et al., 2023). High-fidelity numerical simulations capable of resolving these coupled processes are computationally prohibitive, often requiring weeks of supercomputing time for a single operating condition (Powers et al., 2026). This computational burden fundamentally limits systematic design exploration, uncertainty quantification, and control-oriented modeling. To address these challenges, reduced-order physics-based models have been developed to capture the dominant detonation-front dynamics at dramatically reduced cost (Koch et al., 2021; Koch & Kutz, 2020; Mendible et al., 2021). Among these, the one-dimensional rotating detonation model of Koch and collaborators has emerged as a widely used surrogate for azimuthal detonation propagation (Koch & Kutz, 2020). While such models accurately represent leading-order detonation physics, they necessarily omit or heavily simplify injector dynamics, mixing processes, time-delay effects, and non-equilibrium losses. As a result, substantial and systematically structured discrepancies persist between low-order model predictions and real experimental RDE data. We show that we can leverage Koch’s cheap simulation model (minutes) to approximate simulations of the rich model (weeks), thus allowing for a Cheap2Rich algorithm whereby cheap proxies can be used to model the exceptionally rich multiscale physics observed in reality.

On a three-wave co-rotating configuration (See Fig. 2), the learned LF model remains close to the simple Koch’s model prior and cannot reproduce injector-driven variability. Adding a learned HF pathway reduces the error (an 80.9% reduction) while exhibiting sparse Fourier content concentrated at harmonics of the three-wave structure, indicating phase-locked corrections tied to detonation-front passage and consistent with injector-modulated forcing absent in the baseline model. This yields a practical Cheap2Rich bridge: the reduced model runs in seconds, and the trained network performs full-state reconstruction from sparse measurements at negligible marginal cost compared to high-fidelity simulation, while the structured HF term provides direct access to the subsequent missing-physics identification (e.g., via SINDy (Brunton et al., 2016)).

2. Preliminaries

2.1. RDEs - high fidelity simulation

There has been a lot of prior work on accurate modeling of RDEs that stem from high-fidelity numerical simulations (Raman et al., 2023). In this work, a high-fidelity simulation of the AFRL methane-oxygen rotating detonation rocket engine (RDRE) was studied as shown in Fig.1. This geometry was chosen due to the high availability of experimental (Bennewitz et al., 2019) and numerical simulations (Prakash et al., 2021) available. The reacting compressible Navier-

Stokes and species transport equations (1) are solved using an in-house compressible flow solver (Sharma et al., 2024) built on the AMReX library (Zhang et al., 2019), which provides the adaptive mesh refinement (AMR) framework.

for $k = 1, \dots, N_s$ where ρ is the density of the fluid, t is time, x_i and u_i are the spatial coordinate and the velocity component in the i^{th} direction, respectively. The viscous stress tensor is given as τ_{ij} and p is the fluid pressure. The total chemical energy is defined as e , h is the total enthalpy of the mixture, α is the thermal conductivity of the mixture, D is the diffusivity, and T is the temperature. The mass fraction and chemical source term for the k^{th} species are given by Y_k and Ω_k , respectively. These equations are solved in a Cartesian coordinate system using a second-order finite-volume discretization method, and time integration is performed using a strong stability-preserving second-order Runge–Kutta scheme. Detailed finite-rate chemistry is simulated using Cantera with the FFCMy-12 mechanism (Smith et al., 2016; Xu & Wang, 2018) consisting of 12 species and 38 reactions. For additional details on the numerics and implementation, the reader is referred to (Sharma et al., 2024; Carreon et al., 2025; Bielawski et al., 2023).

The high-fidelity simulation employs a nonuniform grid. A fine resolution of $93.6 \mu\text{m}$ is used in the injectors, plenums, lower half of the combustion chamber, and in the regions containing the detonation wave. The grid is coarsened to $374 \mu\text{m}$ in the upper half of the combustion chamber and further to $748 \mu\text{m}$ in the exhaust plenum. The detonation wave is dynamically tagged using the same pressure gradient threshold as (Powers et al., 2026). The resulting cell count for the simulation was 178 million cells and was run using 3500 CPUs. The simulation cost more than 2 million CPU hours and ran for over 2 months. This simulation required 3.2 billion degrees of freedom.

To ignite the RDRE, four high temperature/pressure kernels were equally spaced in the domain and allowed to evolve. After 0.7 ms the simulation reached steady-state and produced three co-rotating waves. The simulation was allowed to continue for additional 0.5 ms of data collection for averaging. Figure 1 shows the unwrapped view that highlights the temperature and pressure contours. Also, the dynamic tagging of the detonation waves are shown in the 3D geometry. 250 snapshots are considered for the following analysis which corresponds to one full rotation of the waves in the detonation annulus. We then project the AMR results first onto a fixed 3d cylindrical mesh with 30000 points and then on a 1d ring with 100 points at the distance from injectors of 20mm (See Appendix A).

2.2. Koch’s One-Dimensional RDE Model

The model described in (Koch & Kutz, 2020) is a 1D model of the reactive Euler equations with source terms represent-

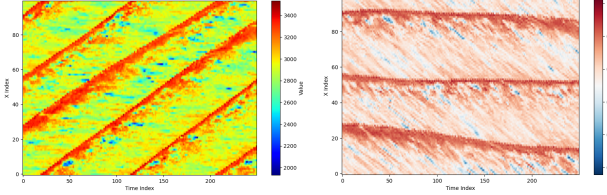


Figure 3. Time evolution of 1d projection of temperature contour before preprocessing (left), and in the COM frame of reference after min-max rescaling (right)

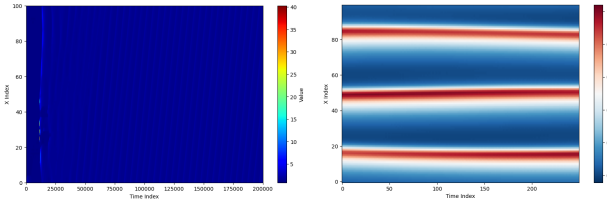


Figure 4. Temperature field obtained from Koch's model described in Subsection 2.2 before (left) and after (right) preprocessing.

$$\begin{aligned}
 \frac{\partial \rho}{\partial t} + \frac{\partial(\rho u_i)}{\partial x_i} &= 0, \\
 \frac{\partial(\rho u_i)}{\partial t} + \frac{\partial(\rho u_i u_j)}{\partial x_j} &= -\frac{\partial p}{\partial x_i} + \frac{\partial \tau_{ij}}{\partial x_j}, \\
 \frac{\partial(\rho e)}{\partial t} + \frac{\partial(\rho h u_j)}{\partial x_j} &= \frac{\partial}{\partial x_j} \left(\alpha \frac{\partial T}{\partial x_j} \right) + \frac{\partial(u_i \tau_{ij})}{\partial x_j} \\
 &\quad + \sum_{k=1}^{N_s} h_k \frac{\partial}{\partial x_j} \left(\rho D \frac{\partial Y_k}{\partial x_j} \right), \\
 \frac{\partial(\rho Y_k)}{\partial t} + \frac{\partial(\rho Y_k u_j)}{\partial x_j} &= \frac{\partial}{\partial x_j} \left(\rho D \frac{\partial Y_k}{\partial x_j} \right) + \Omega_k
 \end{aligned} \quad (1)$$

ing injection, mixing, and chemical kinetics inside an RDE combustion chamber. We describe the model in detail in the appendix B. With the set of parameters described in 2 it is able to model the three co-rotating waves we observe in the high-fidelity simulation. We select time indices [100000, 110000] which correspond to roughly one rotation of the three waves around the ring, and preprocess them by first subsampling them by taking every 400-th snapshot, leaving exactly 250 timesteps which exactly corresponds to the setting of the high-fidelity simulation. We then cancel out the rotation and scale the temperature field to [0, 1] linearly, obtaining the spatio-temporal field in Fig. 4.

3. Cheap2Rich Pipeline

We propose a multi-scale data assimilation framework that decomposes the full-state reconstruction into an additive low-frequency (LF) backbone and a spectrally-constrained high-frequency (HF) residual. This Cheap2Rich architecture leverages the SHRED and DA-SHRED framework

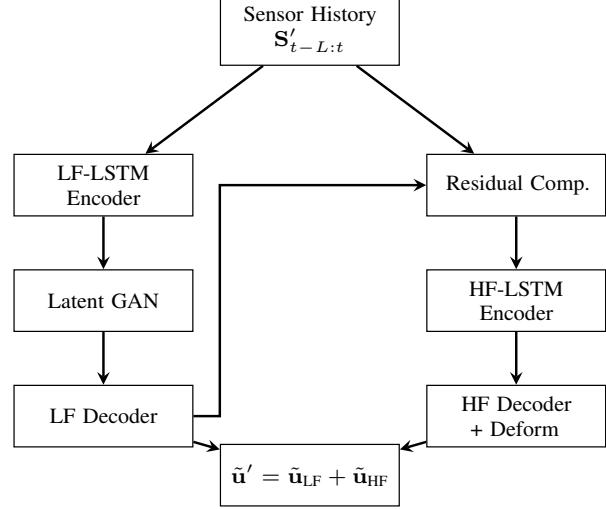


Figure 5. Schematic of the Cheap2Rich architecture. The LF pathway learns the dominant dynamics from simulation and aligns to reality via a latent GAN. The HF pathway learns spectrally-sparse corrections from sensor residuals.

(Williams et al., 2024; Bao & Kutz, 2025) to bridge the simulation-to-reality gap by separating the dominant dynamics captured by simplified models from the fine-scale corrections that account for missing physics. The key insight is that enforcing spectral sparsity on the HF correction encourages physically interpretable, parsimonious representations of the discrepancy (Brunton et al., 2016).

3.1. Problem Setup

We summarize the notation used throughout this section in Table 3 (Appendix C), following the conventions established in (Bao & Kutz, 2025). The full-state reconstruction is decomposed as

$$\tilde{u}'(t) = \tilde{u}_{\text{LF}}(t) + \tilde{u}_{\text{HF}}(t), \quad (2)$$

where \tilde{u}_{LF} captures the dominant low-frequency structure learned from simulation and adapted to reality via latent-space alignment, and \tilde{u}_{HF} represents a spectrally-sparse high-frequency correction. The Cheap2Rich architecture consists of two parallel pathways that process the sensor time-history $\{s'_{t-\ell}\}_{\ell=0}^{L-1}$ with L temporal lags, as illustrated in Figure 5.

3.2. Low-Frequency Pathway

The LF pathway follows the standard DA-SHRED methodology (Bao & Kutz, 2025), consisting of a temporal encoder trained on simulation data and a latent-space alignment.

3.2.1. TEMPORAL ENCODER

Given sensor history $\mathbf{S}'_{t-L:t} = [\mathbf{s}'_{t-L+1}, \dots, \mathbf{s}'_t] \in \mathbb{R}^{L \times p}$, the LF encoder maps this sequence to a latent representation

with a two-layer LSTM (Hochreiter & Schmidhuber, 1997):

$$\mathbf{z}_{\text{LF}}(t) = \mathcal{E}_{\text{LF}}(\mathbf{S}'_{t-L:t}; \theta_{\text{enc}}) = \text{LayerNorm} \left(\mathbf{h}_L^{(2)} \right), \quad (3)$$

where $\mathbf{h}_L^{(2)} \in \mathbb{R}^{d_z}$ is the final hidden state of the second LSTM layer with hidden dimension d_z , and LayerNorm denotes normalization for training stability (Ba et al., 2016).

3.2.2. LATENT-SPACE ALIGNMENT VIA GAN

To bridge the distribution shift between simulation-trained latent codes and those induced by real sensor measurements, we employ a residual generator network \mathcal{G} that learns to align the latent distributions:

$$\tilde{\mathbf{z}}_{\text{LF}}(t) = \mathbf{z}_{\text{LF}}(t) + \mathcal{G}(\mathbf{z}_{\text{LF}}(t); \theta_G). \quad (4)$$

The generator $\mathcal{G} : \mathbb{R}^{d_z} \rightarrow \mathbb{R}^{d_z}$ is a shallow MLP with LeakyReLU activations, initialized to output near-zero corrections. A discriminator network $\mathcal{D} : \mathbb{R}^{d_z} \rightarrow [0, 1]$ is trained adversarially (Goodfellow et al., 2014) to distinguish between latent codes from simulation and transformed codes from real data:

$$\mathcal{L}_D = -\mathbb{E}_{\mathbf{z} \sim p_{\text{sim}}} [\log \mathcal{D}(\mathbf{z})] - \mathbb{E}_{\mathbf{z} \sim p_{\text{sim}}} [\log(1 - \mathcal{D}(\tilde{\mathbf{z}}))], \quad (5)$$

$$\mathcal{L}_G = -\mathbb{E}_{\mathbf{z} \sim p_{\text{sim}}} [\log \mathcal{D}(\tilde{\mathbf{z}})], \quad (6)$$

where $\tilde{\mathbf{z}} = \mathbf{z} + \mathcal{G}(\mathbf{z})$ for \mathbf{z} sampled from simulation latents, and the discriminator is trained to classify real sensor latents as real and generator-transformed simulation latents as fake.

3.2.3. LF DECODER WITH SPECTRAL CONSTRAINT

The aligned latent code is decoded and then low-pass filtered to enforce the low-frequency constraint:

$$\tilde{\mathbf{u}}_{\text{LF}}(t) = \mathcal{P}_{k_c}(\mathcal{D}_{\text{LF}}(\tilde{\mathbf{z}}_{\text{LF}}(t); \theta_{\text{dec}})) \in \mathbb{R}^n, \quad (7)$$

where \mathcal{D}_{LF} is a three-layer MLP with ReLU activations, and \mathcal{P}_{k_c} denotes a low-pass filter that retains only Fourier modes with wavenumber $k \leq k_c$:

$$\mathcal{P}_{k_c}(\mathbf{u}) = \mathcal{F}^{-1}(\mathbf{1}_{k \leq k_c} \cdot \mathcal{F}(\mathbf{u})), \quad (8)$$

where \mathcal{F} and \mathcal{F}^{-1} denote the discrete Fourier transform and its inverse. This explicit spectral constraint separates LF and HF components (Canuto et al., 2006).

3.3. High-Frequency Pathway

The HF pathway is designed to capture the fine-scale discrepancy between the LF reconstruction and reality. The input to the HF pathway is the sensor-space residual between observed measurements and LF predictions at sensor locations. Let $\mathbf{M} \in \mathbb{R}^{p \times n}$ denote the sensor sampling operator. The residual history is computed by subtracting the

current LF prediction (at sensor locations) from each lag of the sensor history:

$$\mathbf{r}_t = \mathbf{s}'_t - \mathbf{M}\tilde{\mathbf{u}}_{\text{LF}}(t), \quad t = 0, 1, \dots, m-1, \quad (9)$$

yielding the residual time-history $\mathbf{R}_{t-L:t} = [\mathbf{r}_{t-L+1}, \dots, \mathbf{r}_t] \in \mathbb{R}^{p \times L}$. Note that each lag uses its corresponding LF prediction $\tilde{\mathbf{u}}_{\text{LF}}(t - \ell)$, ensuring the residual captures the discrepancy between observed and predicted states at each time step.

The HF encoder employs an attention mechanism over temporal lags (Bahdanau et al., 2014) to learn which timesteps are most informative for predicting the HF correction, with time-derivative embedding to capture velocity and acceleration information (see Appendix D). The HF decoder generates a base spatial pattern and applies a learned spatially-varying deformation to correct for velocity mismatches.

3.4. Training Pipeline

The Cheap2Rich model is trained in four sequential stages to ensure stable learning of each component: (1) SHRED training on simulation data, (2) latent GAN training for distribution alignment, (3) HF-SHRED training with spectral sparsity regularization, and (4) fine-tuning. Complete training details including loss functions and hyperparameters are provided in Appendix E.

3.5. Physical Interpretation

The multi-scale decomposition has a natural physical interpretation in the context of RDE dynamics: **LF Component:** Captures the dominant detonation front dynamics that are well-represented by simplified models (e.g., Koch’s model). The low-pass filter \mathcal{P}_{k_c} ensures this component contains only large-scale spatial structures with wavenumber $k \leq k_c$. **HF Component:** Represents fine-scale corrections due to unmodeled injector dynamics, mixing processes, and turbulent fluctuations. The spectral sparsity regularization encourages the discovery of parsimonious, dominant correction modes, while the bandlimited penalty discourages energy at very high frequencies. **Time-Delay Embedding:** The temporal derivative augmentation and attention mechanism allow the HF pathway to capture velocity and phase information from the sensor history, enabling correction of wave propagation mismatches between simulation and reality.

4. Results

We evaluate the Cheap2Rich framework on the rotating detonation engine dataset described in Section 2. The high-fidelity simulation data, which resolves the full three-dimensional reacting flow including shock dynamics, chemical kinetics, and injector interactions, requires weeks of supercomputer time to generate for a single operating con-

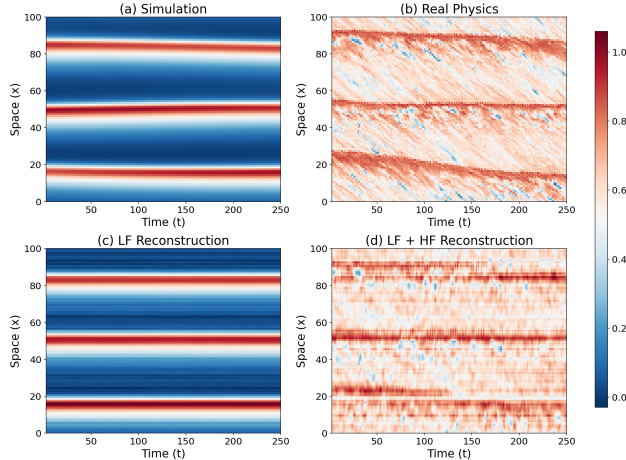


Figure 6. Comparison on the full dataset. (a) Koch’s model simulation capturing dominant front physics. (b) High-fidelity real physics with complex injector-driven dynamics. (c) LF reconstruction from the GAN-aligned SHRED pathway. (d) Full Cheap2Rich LF+HF reconstruction.

dition. In contrast, Koch’s one-dimensional model captures only the dominant detonation front propagation and can be computed in seconds. Our goal is to demonstrate that Cheap2Rich can bridge this fidelity gap using only sparse sensor measurements from the high-fidelity simulation, without requiring access to its full state.

4.1. Experimental Setup

The dataset consists of $m = 250$ temporal snapshots over a spatial domain discretized into $n = 100$ grid points. We use $p = 25$ uniformly distributed sensors and a temporal lag window of $L = 25$ time steps. The data is split into 80% for training and 20% for validation. The cutoff frequency for spectral constraints is set to $k_c = 12$. The training follows a three-stage pipeline: (1) SHRED pretraining on Koch’s model simulation, (2) LF-DA-SHRED with latent GAN alignment, and (3) HF training with spectral sparsity ($\lambda = 0.1$, then fine-tuned with $\lambda' = 0.01$).

4.2. Reconstruction Performance

Figure 6 presents a qualitative comparison of the reconstruction pipeline. The Koch’s model simulation (panel a) captures the three co-rotating detonation fronts but exhibits smooth, idealized dynamics. The high-fidelity simulation (panel b) reveals substantially richer structure: the detonation fronts display spatial variability, and significant fine-scale fluctuations arise from injector dynamics, mixing processes, and turbulent interactions that are absent in the simplified model. The LF reconstruction (panel c) produces output that closely mirrors the Koch’s model, as expected since the LF pathway is trained on simulation data. Despite the GAN-based latent alignment, the LF component

Method	RMSE (Valid)	SSIM
Sim2Real Gap	0.4110	0.1038
LF-DA-SHRED	0.4114	0.1113
Cheap2Rich	0.1031	0.3638
Improvement	74.9%	250.5%

Table 1. Reconstruction comparison. The Cheap2Rich framework achieves substantial improvement by learning spectrally-sparse corrections from sensor residuals - detailed comparison to other baseline approaches in F.

alone cannot capture the fine-scale discrepancies, yielding an RMSE of 0.4114. The full Cheap2Rich LF+HF reconstruction (panel d) successfully recovers the complex dynamics of the high-fidelity simulation, reducing the RMSE to 0.1031—an improvement of 74.9%.

4.3. Quantitative Analysis

Table 1 summarizes the reconstruction performance. The baseline SHRED model trained on simulation and applied directly to real sensor data performs poorly due to the distribution shift. The GAN alignment provides minimal improvement for the LF pathway alone, indicating that the dominant discrepancy lies in unmodeled physics rather than latent distribution mismatch. The HF correction provides the critical improvement, reducing reconstruction error by over 74% on the held-out validation set.

4.4. Spectral Analysis of the HF Correction

Figure 7 provides detailed analysis of the multi-scale decomposition. The top-left panel shows that the LF reconstruction fails to track the high-fidelity ground truth, while the top-right panel demonstrates that the full Cheap2Rich LF+HF reconstruction closely follows the true dynamics. The bottom-left panel compares the predicted HF component against the true residual (ground truth minus LF prediction), showing good agreement in both amplitude and phase. The bottom-right panel reveals the spectral structure of the learned HF correction. The frequency content is sparse and concentrated at wavenumbers $k \in \{3, 6, 9, 11\}$, with the dominant modes at $k = 3, 6, 9$ corresponding to harmonics of the three co-rotating detonation waves. This physically interpretable structure emerges automatically from the spectral sparsity regularization, suggesting that the HF pathway has learned to represent the injector-driven physics in terms of modes that are commensurate with the underlying waves.

4.5. Physical Interpretation

The results demonstrate that the method successfully decomposes the Cheap2Rich gap into interpretable components:

Front Physics (LF Component). The LF pathway, trained on Koch’s model data and aligned via the latent GAN, cap-

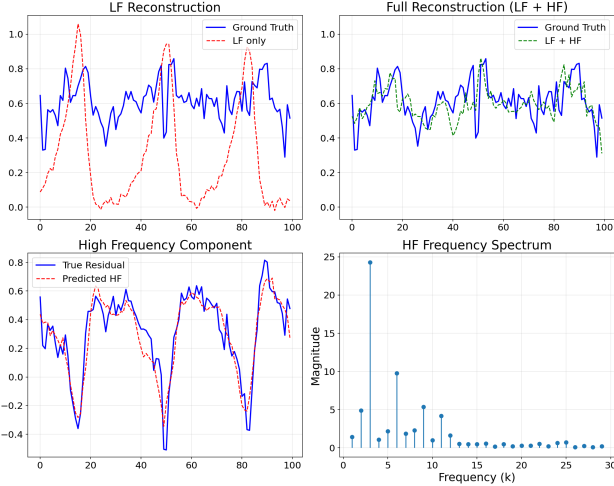


Figure 7. Detailed analysis of multi-scale reconstruction. Top-left: LF reconstruction versus ground truth at a representative spatial slice. Top-right: Cheap2Rich LF+HF reconstruction. Bottom-left: Predicted HF component compared to the true residual. Bottom-right: Frequency spectrum of the HF correction showing sparse structure concentrated at wavenumbers $k \in \{3, 6, 9\}$.

tures the dominant detonation front locations and propagation speeds. The three co-rotating fronts are clearly visible in both the simulation and LF reconstruction, confirming that the simplified model adequately represents the leading-order dynamics.

Injector Physics (HF Component). The HF correction captures the fine-scale dynamics that arise from physics absent in the Koch’s model: injector response delays, spatially varying mixing efficiency (Schwer & Kailasanath, 2010), and local turbulent fluctuations (Fotia et al., 2016). These effects manifest as structured corrections concentrated near the detonation fronts and in the inter-front regions where fresh reactants are injected.

The sparse spectral structure of the HF component—with energy concentrated at harmonics of the fundamental three-wave mode—suggests that the injector-driven physics are phase-locked to the detonation front passage. This is physically consistent with the periodic pressure fluctuations that modulate injector flow rates as each detonation wave passes.

4.6. Computational Implications

The Cheap2Rich framework enables high-fidelity state reconstruction at dramatically reduced computational cost. While the original high-fidelity simulation requires weeks of supercomputer time, our approach requires only sparse sensor measurements from the real system, a low-fidelity baseline model (e.g., Koch’s model) that runs in seconds, and lightweight neural network inference that runs in minutes on a standard laptop without requiring GPU clusters. This enables rapid exploration of the RDE design space, where each new operating condition can be characterized

through sparse sensing rather than expensive full-scale simulation. The learned HF corrections provide interpretable diagnostics of injector performance without requiring direct measurement of the full injection dynamics.

5. Discovery of Missing Physics via SINDy

Beyond closing the simulation-to-reality gap through reconstruction, the Cheap2Rich framework enables explicit identification of the missing physics terms that account for the discrepancy between the simplified Koch’s model and high-fidelity dynamics. Following the methodology established in (Bao & Kutz, 2025), we employ sparse identification of nonlinear dynamics (SINDy) (Rudy et al., 2017) within DA-SHRED architecture to discover interpretable governing equations for the learned corrections. The core insight is that the multi-scale decomposition provides natural targets for physics discovery: the LF correction dynamics, the HF component dynamics, and the direct missing physics (see Appendix G for the complete SINDy framework and library construction details).

5.1. Discovered Equations

Applying SINDy to the Cheap2Rich outputs yields the following discovered equations.

Known Baseline: Koch’s Model. For reference, the simplified Koch’s model governing the simulation takes the form:

$$\frac{\partial u}{\partial t} + u \frac{\partial u}{\partial x} = q \cdot k(1 - \lambda) \exp\left(\frac{u - u_c}{\alpha}\right) - \epsilon u^2, \quad (10)$$

which captures the detonation front propagation through nonlinear advection and Arrhenius-type reaction kinetics.

Discovered: LF Correction. The GAN alignment contributes the following correction to the simulation dynamics:

$$\begin{aligned} \frac{\partial}{\partial t} (u_{\text{LF}} - u_{\text{sim}}) = & -0.048 \Delta u + 0.005 u_{\text{LF}} - 0.013 u_{\text{LF}}^2 \\ & - 0.056 u_{\text{LF}} \cdot \Delta u + \mathcal{O}(\partial_x). \end{aligned} \quad (11)$$

The dominant terms are polynomial in u_{LF} and the correction $\Delta u = u_{\text{LF}} - u_{\text{sim}}$, suggesting that the GAN primarily adjusts the amplitude and baseline of the reconstruction rather than its spatial structure.

Discovered: HF Dynamics. The high-frequency component evolves according to:

$$\begin{aligned} \frac{\partial u_{\text{HF}}}{\partial t} = & 0.018 - 0.029 u_{\text{HF}} - 0.018 u_{\text{LF}} \\ & - 0.067 u_{\text{LF}} \cdot u_{\text{HF}} + 0.151 u_{\text{LF}}^2 \cdot u_{\text{HF}} + \mathcal{O}(\partial_x). \end{aligned} \quad (12)$$

The coupling terms $u_{\text{LF}} \cdot u_{\text{HF}}$ and $u_{\text{LF}}^2 \cdot u_{\text{HF}}$ indicate that the HF dynamics are modulated by the LF wave structure, consistent with the physical picture of injector-driven fluc-

tuations being phase-locked to detonation front passage.

Discovered: Direct Missing Physics. The total discrepancy between real and simulated dynamics (10) is governed by:

$$\begin{aligned} \frac{\partial}{\partial t} (u_{\text{real}} - u_{\text{sim}}) = & 0.723 - 3.79 u + 6.24 u^2 - 3.33 u^3 \\ & + 0.403 u_x - 0.404 u \cdot u_x + \mathcal{O}(u_{xx}). \end{aligned} \quad (13)$$

5.2. Physical Interpretation of Discovered Terms

We discovered interpretable corrections to Koch’s model, with each term addressing different physical mechanisms.

Front Physics Corrections. The direct missing physics equation (13) exhibits Burgers-type structure: a polynomial source term correcting reaction kinetics and advection terms adjusting wave speeds. The cubic polynomial $-3.79u + 6.24u^2 - 3.33u^3$ modifies the effective Arrhenius reaction rates, while $0.40u_x - 0.40u \cdot u_x$ corrects detonation front propagation. These terms primarily address deficiencies in Koch’s representation of front physics.

Injector Physics via LF-HF Coupling. The HF dynamics equation (12) captures a different mechanism through the coupling terms $u_{\text{LF}} \cdot u_{\text{HF}}$ and $u_{\text{LF}}^2 \cdot u_{\text{HF}}$. This nonlinear modulation explains the observations from Section 4: HF corrections concentrate near detonation fronts and exhibit spectral sparsity at $k \in \{3, 6, 9\}$. The coupling ensures HF fluctuations are amplified in phase with the three-wave LF structure, consistent with injector-driven physics being modulated by periodic pressure fluctuations.

The discovered equations provide pathways for improving the Koch’s model without requiring the neural network at inference time. Both direct correction using (13) and hierarchical correction using the LF and HF terms separately are possible; details are provided in Appendix G.

6. Conclusions and Future Works

This work presents a multi-scale data assimilation framework for rotating detonation engines that successfully bridges the sim2real gap between low-fidelity proxy models and complex coupled physics. The proposed Cheap2Rich architecture decomposes the reconstruction task into a low-frequency pathway, which captures dominant detonation front dynamics through GAN-aligned latent representations, and a high-frequency pathway that learns spectrally-sparse corrections from sensor residuals. Applied to a three-wave co-rotating RDE configuration, the framework achieves 80.9% reduction in reconstruction RMSE while requiring only 25 sparse sensor measurements and lightweight neural network inference without GPU clusters. Spectral analysis reveals that the learned HF corrections exhibit sparse structure, with energy concentrated at harmonics of the fundamental three-wave mode, providing physically inter-

pretable representations of injector-driven physics absent from the baseline proxy model. Furthermore, the application of SINDy to the multi-scale decomposition yields explicit governing equations for the missing physics, distinguishing between front physics corrections of Burgers type and injector physics captured through LF-HF coupling terms. These discovered functionals offer actionable pathways for improving reduced-order simulations.

Several promising directions emerge from this work. First, the trained Cheap2Rich model constitutes a computationally efficient surrogate that could enable gradient-based design optimization of RDE geometry, injector placement, and operating conditions at negligible computational cost compared to full-scale simulation. Such surrogate-driven optimization (Forrester et al., 2008) would dramatically accelerate the exploration of high-performance engine configurations that currently require prohibitive computational resources. Second, Cheap2Rich’s ability for full-state reconstruction from sparse real-time sensor measurements suggests potential applications in closed-loop control of RDE systems. By coupling the surrogate model with reinforcement learning algorithms (Rabault et al., 2019), one could develop controllers that modulate injector mass flow rates (Fotia et al., 2016) to guarantee stable detonation with a prescribed number of waves (Bennewitz et al., 2018), addressing a critical challenge in transitioning RDE technology from laboratory demonstrations to operational propulsion systems. Third, while present work demonstrates Cheap2Rich on 1D RDE dynamics, extension to higher-dimensional spatiotemporal fields presents additional challenges that require substantial architectural innovations. Recent work has extended the LF/HF decomposition to 2D remote sensing applications using a hierarchical peeling structure, where the targets exhibit fundamentally different characteristics from the structured physics considered here: vegetation index reconstruction involves heterogeneous landscapes with sharp discontinuities, non-stationary spatial statistics, and irregular temporal dynamics without a physically well-established prior. Its success demonstrates that the Cheap2Rich paradigm has broader applicability beyond combustion physics and to higher dimensions—in turbulent flows, climate monitoring, and atmospheric modeling—where multi-fidelity approaches could dramatically reduce the computational burden of high-resolution simulation while preserving physically meaningful fine-scale structure. Fourth, the latent-space representations provide a natural foundation for autoregressive forecasting, wherein dynamics are evolved cheaply in the compressed space and subsequently decoded to full three-dimensional fields. Integrating SINDy-discovered dynamics into such a latent forecasting architecture (Champion et al., 2019) could yield interpretable, long-horizon predictions that maintain physical consistency (Vlachas et al., 2022).

Impact Statement

In this paper we investigate the applications of Machine Learning to the frontier of propulsion engineering - rotating detonation engines. The current bottlenecks in the design and engineering of RDEs stem from prohibitive simulation costs and our work demonstrates progress in finding inexpensive surrogate models which allow for design and control of these systems. Societal impacts from advancing propulsion technology are likely to increase humanity's footprint beyond Earth, but the same technologies can serve national security goals of various states.

Acknowledgments

LLMs from OpenAI and Anthropic have been used in preparation of the code and corrections to the manuscript. This work was supported in part by the US National Science Foundation (NSF) AI Institute for Dynamical Systems (dynamicsai.org), grant 2112085. JNK further acknowledges support from the Air Force Office of Scientific Research (FA9550-24-1-0141). The authors also acknowledge from the AFOSR/AFRL Center of Excellence in Assimilation of Flow Features in Compressible Reacting Flows under award number FA9550-25-1-0011, monitored by Dr. Chipping Li and Dr. Ramakanth Munipalli. MP acknowledges support from the National Defense Science and Engineering Graduate (NDSEG) Fellowship, USA through the Air Force Research Laboratory (AFRL).

References

Ba, J. L., Kiros, J. R., and Hinton, G. E. Layer normalization. *arXiv preprint arXiv:1607.06450*, 2016.

Bahdanau, D., Cho, K., and Bengio, Y. Neural machine translation by jointly learning to align and translate. *arXiv preprint arXiv:1409.0473*, 2014.

Bao, Y. and Kutz, J. N. Data assimilation and discrepancy modeling with shallow recurrent decoders. *arXiv preprint arXiv:2512.01170*, 2025.

Bennewitz, J. W., Valentini, D., Plascencia, M. A., Vargas, A., Sim, H. S., Lopez, B., Smith, O. I., and Karagozian, A. R. Periodic partial extinction in acoustically coupled fuel droplet combustion. *Combustion and flame*, 189: 46–61, 2018.

Bennewitz, J. W., Bigler, B. R., Pilgram, J. J., and Hargus Jr, W. A. Modal transitions in rotating detonation rocket engines. *International Journal of Energetic Materials and Chemical Propulsion*, 18(2), 2019.

Bielawski, R., Barwey, S., Prakash, S., and Raman, V. Highly-scalable gpu-accelerated compressible reacting flow solver for modeling high-speed flows. *Computers & Fluids*, 265:105972, 2023.

Bocquet, M., Brajard, J., Carrassi, A., and Bertino, L. Data assimilation as a learning tool to infer ordinary differential equation representations of dynamical models. *Nonlinear Processes in Geophysics*, 26(3):143–162, 2019. doi: 10.5194/npg-26-143-2019. URL <https://npg.copernicus.org/articles/26/143/2019/>.

Brunton, S. L. and Kutz, J. N. *Data-driven science and engineering: Machine learning, dynamical systems, and control*. Cambridge University Press, 2022.

Brunton, S. L., Proctor, J. L., and Kutz, J. N. Discovering governing equations from data by sparse identification of nonlinear dynamical systems. *Proceedings of the national academy of sciences*, 113(15):3932–3937, 2016.

Canuto, C., Hussaini, M. Y., Quarteroni, A., and Zang, T. A. *Spectral methods: fundamentals in single domains*. Springer, 2006.

Carreon, A., Singh, J., Sharma, S., Zhang, S., and Raman, V. A gpu-based compressible combustion solver for applications exhibiting disparate space and time scales. 10 2025. doi: 10.48550/arXiv.2510.23993.

Champion, K., Lusch, B., Kutz, J. N., and Brunton, S. L. Data-driven discovery of coordinates and governing equations. *Proceedings of the National Academy of Sciences*, 116(45):22445–22451, 2019.

Erichson, N. B., Mathelin, L., Yao, Z., Brunton, S. L., Mahoney, M. W., and Kutz, J. N. Shallow neural networks for fluid flow reconstruction with limited sensors. *Proceedings of the Royal Society A*, 476(2238):20200097, 2020.

Fan, Z., Sun, Y., Yang, S., and Lu, Y. Physics-informed inference time scaling via simulation-calibrated scientific machine learning. *arXiv preprint arXiv:2504.16172*, 2025.

Forrester, A., Sobester, A., and Keane, A. *Engineering design via surrogate modelling: a practical guide*. John Wiley & Sons, 2008.

Fotia, M. L., Schauer, F., Kaemming, T., and Hoke, J. Experimental study of the performance of a rotating detonation engine with nozzle. *Journal of Propulsion and Power*, 32 (3):674–681, 2016.

Ghil, M. and Malanotte-Rizzoli, P. Data assimilation in meteorology and oceanography. volume 33 of *Advances in Geophysics*, pp. 141–266. Elsevier, 1991. doi: [https://doi.org/10.1016/S0065-2687\(08\)60442-2](https://doi.org/10.1016/S0065-2687(08)60442-2). URL <https://www.sciencedirect.com/science/article/pii/S0065268708604422>.

Goodfellow, I. J., Pouget-Abadie, J., Mirza, M., Xu, B., Warde-Farley, D., Ozair, S., Courville, A., and Bengio, Y. Generative adversarial nets. In *Proceedings of the 28th International Conference on Neural Information Processing Systems - Volume 2, NIPS'14*, pp. 2672–2680, Cambridge, MA, USA, 2014. MIT Press.

Hochreiter, S. and Schmidhuber, J. Long short-term memory. *Neural computation*, 9(8):1735–1780, 1997.

Jiang, R., Zhang, X., Jakhar, K., Lu, P. Y., Hassanzadeh, P., Maire, M., and Willett, R. Hierarchical implicit neural emulators. *arXiv preprint arXiv:2506.04528*, 2025.

Karniadakis, G. E., Kevrekidis, I. G., Lu, L., Perdikaris, P., Wang, S., and Yang, L. Physics-informed machine learning. *Nature Reviews Physics*, 3(6):422–440, 2021.

Ketcheson, D. I., Mandli, K. T., Ahmadia, A. J., Alghamdi, A., Quezada de Luna, M., Parsani, M., Knepley, M. G., and Emmett, M. PyClaw: Accessible, Extensible, Scalable Tools for Wave Propagation Problems. *SIAM Journal on Scientific Computing*, 34(4):C210–C231, November 2012.

Koch, J. and Kutz, J. N. Modeling thermodynamic trends of rotating detonation engines. *Physics of Fluids*, 32(12):126102, 12 2020. ISSN 1070-6631. doi: 10.1063/5.0023972. URL <https://doi.org/10.1063/5.0023972>.

Koch, J., Kurosaka, M., Knowlen, C., and Kutz, J. N. Multiscale physics of rotating detonation waves: Auto-solitons and modulational instabilities. *Phys. Rev. E*, 104:024210, Aug 2021. doi: 10.1103/PhysRevE.104.024210. URL <https://link.aps.org/doi/10.1103/PhysRevE.104.024210>.

Kutz, J. N., Battaglia, P., Brenner, M., Carlberg, K., Hargberg, A., Ho, S., Hoyer, S., Lange, H., Lipson, H., Mahoney, M. W., et al. Accelerating scientific discovery with the common task framework. *arXiv preprint arXiv:2511.04001*, 2025.

Li, Z., Kovachki, N., Azizzadenesheli, K., Liu, B., Bhattacharya, K., Stuart, A., and Anandkumar, A. Fourier neural operator for parametric partial differential equations. *arXiv preprint arXiv:2010.08895*, 2020.

Liu, Z., Wang, Y., Vaidya, S., Ruehle, F., Halverson, J., Soljačić, M., Hou, T. Y., and Tegmark, M. Kan: Kolmogorov-arnold networks. *arXiv preprint arXiv:2404.19756*, 2024.

Lu, L., Jin, P., Pang, G., Zhang, Z., and Karniadakis, G. E. Learning nonlinear operators via deeponet based on the universal approximation theorem of operators. *Nature machine intelligence*, 3(3):218–229, 2021.

Mendible, A., Koch, J., Lange, H., Brunton, S. L., and Kutz, J. N. Data-driven modeling of rotating detonation waves. *Phys. Rev. Fluids*, 6:050507, May 2021. doi: 10.1103/PhysRevFluids.6.050507. URL <https://link.aps.org/doi/10.1103/PhysRevFluids.6.050507>.

Nakagami, S., Matsuoka, K., Kasahara, J., Kumazawa, Y., Fujii, J., Matsuo, A., and Funaki, I. Experimental visualization of the structure of rotating detonation waves in a disk-shaped combustor. *Journal of Propulsion and Power*, 33(1):80–88, 2017. doi: 10.2514/1.B36084. URL <https://doi.org/10.2514/1.B36084>.

Niu, R., Wu, D., Kim, K., Ma, Y.-A., Watson-Parris, D., and Yu, R. Multi-fidelity residual neural processes for scalable surrogate modeling. *arXiv preprint arXiv:2402.18846*, 2024.

Powers, M., Sharma, S., and Raman, V. *Impact of Varying Combustion Chamber Area in Rotating Detonation Engines*. 2026. doi: 10.2514/6.2026-2613. URL <https://arc.aiaa.org/doi/abs/10.2514/6.2026-2613>.

Prakash, S., Raman, V., Lietz, C. F., Hargus Jr, W. A., and Schumaker, S. A. Numerical simulation of a methane-oxygen rotating detonation rocket engine. *Proceedings of the Combustion Institute*, 38(3):3777–3786, 2021.

Rabault, J., Kuchta, M., Jensen, A., Réglade, U., and Cерди, N. Artificial neural networks trained through deep reinforcement learning discover control strategies for active flow control. *Journal of fluid mechanics*, 865:281–302, 2019.

Rahaman, N., Baratin, A., Arpit, D., Draxler, F., Lin, M., Hamprecht, F., Bengio, Y., and Courville, A. On the spectral bias of neural networks. In *International conference on machine learning*, pp. 5301–5310. PMLR, 2019.

Raman, V., Prakash, S., and Gamba, M. Nonidealities in rotating detonation engines. *Annual Review of Fluid Mechanics*, 55(Volume 55, 2023):639–674, 2023. ISSN 1545-4479. doi: <https://doi.org/10.1146/annurev-fluid-120720-032612>. URL <https://www.annualreviews.org/content/journals/10.1146/annurev-fluid-120720-032612>.

Roy, S., Bahmani, B., Kevrekidis, I. G., and Shields, M. D. A physics-informed multi-resolution neural operator. *arXiv preprint arXiv:2510.23810*, 2025.

Rudy, S. H., Brunton, S. L., Proctor, J. L., and Kutz, J. N. Data-driven discovery of partial differential equations. *Science advances*, 3(4):e1602614, 2017.

Sato, T., Chacon, F., White, L., Raman, V., and Gamba, M. Mixing and detonation structure in a rotating detonation engine with an axial air inlet. *Proceedings of the Combustion Institute*, 38(3):3769–3776, 2021. ISSN 1540-7489. doi: <https://doi.org/10.1016/j.proci.2020.06.283>. URL <https://www.sciencedirect.com/science/article/pii/S1540748920303758>.

Sato, T., Matsuoka, K., Itouyama, N., Yasui, M., Matsuyama, K., Ide, Y., Nakata, K., Suzuki, Y., Ishibashi, R., Suzuki, S., Kasahara, J., Kawasaki, A., Hirashima, H., Nakata, D., Eguchi, H., Takano, T., Uchiumi, M., Himeno, T., Yahata, Y., and Yamada, K. Space flight of liquid rotating detonation engine using sounding rocket s-520-34. *Journal of Spacecraft and Rockets*, pp. 1–18, 11 2025. doi: 10.2514/1.A36447.

Schwer, D. and Kailasanath, K. Numerical investigation of rotating detonation engines. In *46th AIAA/ASME/SAE/ASEE joint propulsion conference & exhibit*, pp. 6880, 2010.

Sharma, S., Bielawski, R., Gibson, O., Zhang, S., Sharma, V., Rauch, A. H., Singh, J., Abisleiman, S., Ullman, M., Barwey, S., and Raman, V. An amrex-based compressible reacting flow solver for high-speed reacting flows relevant to hypersonic propulsion. *arXiv preprint arXiv:2412.00900*, 2024.

Smith, G. P., Tao, Y., and Wang, H. Foundational fuel chemistry model version 1.0 (ffcm-1). *epub, accessed July, 26:2018*, 2016.

Tomasetto, M., Williams, J. P., Braghin, F., Manzoni, A., and Kutz, J. N. Reduced order modeling with shallow recurrent decoder networks. *Nature Communications*, 16(1):10260, 2025.

Vlachas, P. R., Arampatzis, G., Uhler, C., and Koumoutsakos, P. Multiscale simulations of complex systems by learning their effective dynamics. *Nature Machine Intelligence*, 4(4):359–366, 2022.

Williams, J. P., Zahn, O., and Kutz, J. N. Sensing with shallow recurrent decoder networks. *Proceedings of the Royal Society A: Mathematical, Physical and Engineering Sciences*, 480(2298):20240054, 09 2024. ISSN 1364-5021. doi: 10.1098/rspa.2024.0054. URL <https://doi.org/10.1098/rspa.2024.0054>.

Wolański, P. Detonative propulsion. *Proceedings of the Combustion Institute*, 34(1):125–158, 2013. ISSN 1540-7489. doi: <https://doi.org/10.1016/j.proci.2012.10.005>. URL <https://www.sciencedirect.com/science/article/pii/S1540748912004014>.

Wyder, P. M., Goldfeder, J., Yermakov, A., Zhao, Y., Riva, S., Williams, J. P., Zoro, D., Rude, A. S., Tomasetto, M., Germany, J., et al. Common task framework for a critical evaluation of scientific machine learning algorithms. *arXiv preprint arXiv:2510.23166*, 2025.

Xu, R. and Wang, H. A reduced reaction model of methane combustion: Ffcmy-12. Personal communication, 2018.

Zhang, W., Almgren, A., Beckner, V., Bell, J., Blaschke, J., Chan, C., Day, M., Friesen, B., Gott, K., Graves, D., Katz, M., Myers, A., Nguyen, T., Nonaka, A., Rosso, M., Williams, S., and Zingale, M. Amrex: a framework for block-structured adaptive mesh refinement. *Journal of Open Source Software*, 4:1370, 05 2019. doi: 10.21105/joss.01370.

A. Preprocessing of the High Fidelity Sim

A.1. Interpolation of ADR onto a fixed spatial grid

To map each snapshot from the native (unstructured) simulation point cloud onto a fixed cylindrical reference grid with $3 \times 100 \times 100$ points equally spaced in the r, ϕ, z directions in a cylindrical coordinate system, we build a KD-tree over the source coordinates $\{\mathbf{x}_j\}_{j=1}^{N_s} \subset \mathbb{R}^3$ and, for every target grid point \mathbf{g}_i ($i = 1, \dots, N_g$), query its k nearest neighbors $\mathcal{N}_k(i)$ with Euclidean distances $d_{ij} = \|\mathbf{g}_i - \mathbf{x}_j\|_2$. The field value $v(\mathbf{g}_i)$ is then obtained by inverse-distance weighting with a softened exponent, i.e.,

$$\hat{v}(\mathbf{g}_i) = \sum_{j \in \mathcal{N}_k(i)} w_{ij} v(\mathbf{x}_j), \quad w_{ij} = \frac{(d_{ij} + \varepsilon)^{-1/2}}{\sum_{\ell \in \mathcal{N}_k(i)} (d_{i\ell} + \varepsilon)^{-1/2}},$$

where ε is a small constant for numerical stability; this yields a smooth local interpolation while remaining computationally efficient via batched neighbor queries.

A.2. Projection onto a 1d ring

Finally, we pick $h_* = 20$ mm and take the mean of the three points of the grid at the fixed h_* and $\phi(i) = \frac{i}{100}2\pi$ obtaining a 1d dataset which is presented on Figure 3. After the projection step, we also counter the rotation of the waves by shifting the frame at time index i by $i\frac{2\pi}{250}$ radians, and changing the Temperature scale with a min-max scaler.

B. Koch's Model

The physical system describes a compressible reactive flow where fuel and oxidizer are continuously injected into an annular combustor channel, mix at a rate governed by a mixing parameter s , and undergo chemical reaction according to Arrhenius kinetics with Damköhler number Da and activation energy Ea . The system conserves mass, momentum, energy, and a progress variable (mixture fraction z) that tracks the degree of mixing and reaction. Key physical phenomena include injection through the boundary characterized by an area ratio AR , heat release hv from chemical reactions controlled by an ignition temperature T_{ign} , and a choked flow condition at the injection boundary that depends on the local pressure state. The governing equations employ a gamma-law equation of state with specific heat ratio $\gamma = 1.29$, representative of detonation products, and include Heaviside functions to model activation of injection, chemical reactions, and boundary conditions.

The numerical solution employs a finite volume method with operator splitting to separately handle hyperbolic transport and stiff reactive source terms. The inviscid flux terms are discretized using a second-order Clawpack framework (Ketcheson et al., 2012) with an HLLC (Harten-Lax-van Leer-Contact) Riemann solver that resolves shock waves, contact discontinuities, and expansion fans in the reactive flow field. The source terms arising from injection, mixing, and chemical reaction are integrated using a second-order explicit Runge-Kutta method (RK2) with adaptive time stepping controlled by a CFL condition of 0.1. The chemical source term incorporates a temperature-dependent reaction rate with Arrhenius kinetics, activated only above a threshold temperature of $1.01 \times T_{ign}$ to ensure numerical stability. Periodic boundary conditions are enforced at both domain boundaries to simulate the azimuthal periodicity of the annular combustor, and the simulation tracks primitive variables (density, velocity, pressure, temperature, and mixture fraction) over a domain length of 24 characteristic lengths discretized with 100 grid points, evolving the solution to a final dimensionless time of 180 to capture multiple detonation wave passages and establish quasi-steady periodic behavior.

Four distinct RDE configurations were investigated to demonstrate the universality of the model 8. Just by changing the s parameter in the model we can obtain simulations which have quasi-steady states of one ($s = 0.05$) or two waves ($s = 0.06$), a pulsing detonation ($s = 0.04$), and three waves which correspond to the high-fidelity setting with ($s = 0.07$).

We find a set of parameters which best resemble the data observed in the high resolution 3d simulation. For the following set of parameters we are able to achieve a quasi-steady state of three co-rotating waves 2.

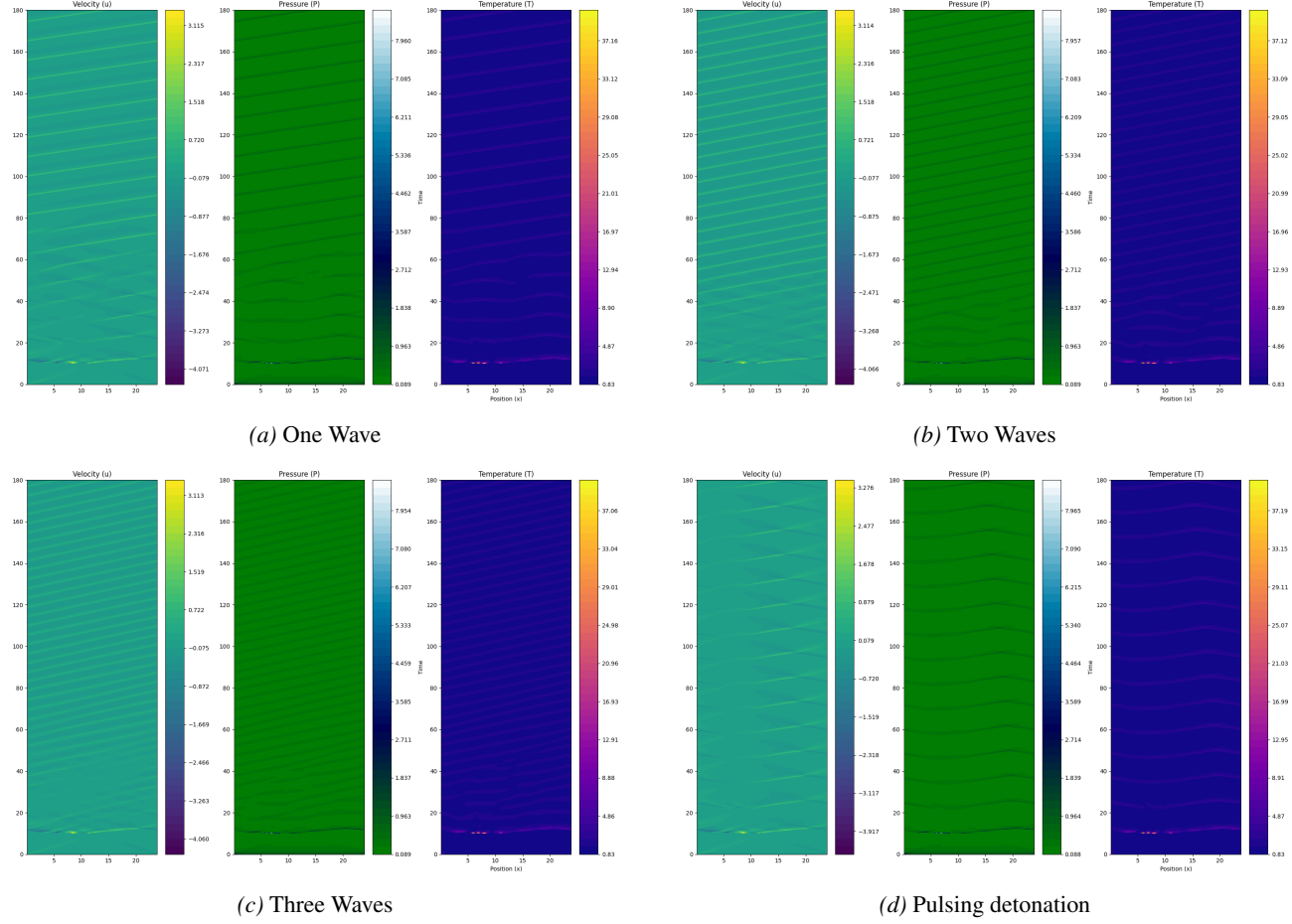


Figure 8. Comparison of four RDE operational modes demonstrating model capacity to simulate different wave structures

C. Notation Summary

See Table 3.

D. High-Frequency Pathway Details

This appendix provides detailed specifications of the high-frequency pathway components described in Section 3.

D.1. Time-Derivative Embedding

To capture velocity and acceleration information critical for correcting phase mismatches, the residual history is augmented with finite-difference temporal derivatives:

$$\dot{\mathbf{r}}_\ell = \frac{\mathbf{r}_{\ell+1} - \mathbf{r}_{\ell-1}}{2\Delta t}, \quad (14)$$

$$\ddot{\mathbf{r}}_\ell = \frac{\mathbf{r}_{\ell+1} - 2\mathbf{r}_\ell + \mathbf{r}_{\ell-1}}{\Delta t^2}, \quad (15)$$

forming an augmented input $\tilde{\mathbf{R}} = [\mathbf{r}_\ell, \dot{\mathbf{r}}_\ell, \ddot{\mathbf{r}}_\ell] \in \mathbb{R}^{L \times 3p}$ that embeds the local temporal structure.

Parameter	Value	Parameter	Value
γ	1.29	Da	289
p_{ref}	1.0	T_{ign}	5.8
ρ_{ref}	1.0	h_v	24.6
R	1.0	E_a	11.5
T_{ref}	1.0	L	24.0
AR	0.2	m_x	100
s	0.07	t_{final}	180.0
β	14.286		

Table 2. Simulation parameters for three co-rotating waves configuration.

	Simulation	Reality
State Space	$\mathbf{u}_k = \mathbf{u}(\mathbf{x}, t_k) \in \mathbb{R}^n$	$\mathbf{u}'_k = \mathbf{u}'(\mathbf{x}, t_k) \in \mathbb{R}^n$
Sensor Data	$\mathbf{s}_k = \mathbf{M}\mathbf{u}_k \in \mathbb{R}^p$	$\mathbf{s}'_k \in \mathbb{R}^p$
Data Matrix	$\mathbf{X} = [\mathbf{u}_1 \cdots \mathbf{u}_m] \in \mathbb{R}^{n \times m}$	$\mathbf{X}' = [\mathbf{u}'_1 \cdots \mathbf{u}'_m] \in \mathbb{R}^{n \times m}$
Sensor Matrix	$\mathbf{S} = [\mathbf{s}_1 \cdots \mathbf{s}_m] \in \mathbb{R}^{p \times m}$	$\mathbf{S}' = [\mathbf{s}'_1 \cdots \mathbf{s}'_m] \in \mathbb{R}^{p \times m}$
Sampling Operator		$\mathbf{M} \in \mathbb{R}^{p \times n}$
Governing Equations	$\mathbf{u}_t = \mathcal{N}(\mathbf{u}, \mathbf{x}, t)$	$\mathbf{u}'_t = \mathcal{M}(\mathbf{u}', \mathbf{x}, t)$

Table 3. Summary of variables, data, and models used in the Cheap2Rich formulation. The state space is of dimension n , there are m snapshots of temporal measurements using p sensors. For reality, only sensor measurements \mathbf{s}'_k are observed; the full state \mathbf{u}'_k is never directly available.

D.2. Temporal Attention Encoder

The HF encoder employs an attention mechanism over temporal lags to learn which timesteps are most informative for predicting the HF correction:

$$\mathbf{H} = \text{LSTM}_{\text{all}}(\tilde{\mathbf{R}}; \boldsymbol{\theta}_{\text{all}}) \in \mathbb{R}^{L \times d_z}, \quad (16)$$

$$\mathbf{h}_{\text{final}} = \text{LayerNorm} \left(\text{LSTM}_{\text{main}}(\tilde{\mathbf{R}}; \boldsymbol{\theta}_{\text{main}}) \right) \in \mathbb{R}^{d_z}, \quad (17)$$

$$\boldsymbol{\alpha} = \text{softmax}(\mathcal{A}(\mathbf{h}_{\text{final}}; \boldsymbol{\theta}_A)) \in \mathbb{R}^L, \quad (18)$$

$$\mathbf{z}_{\text{HF}} = \sum_{\ell=1}^L \alpha_{\ell} \mathbf{H}_{\ell}, \quad (19)$$

where LSTM_{all} returns hidden states at all timesteps, $\text{LSTM}_{\text{main}}$ is a two-layer LSTM returning only the final hidden state, $\mathcal{A} : \mathbb{R}^{d_z} \rightarrow \mathbb{R}^L$ is a two-layer attention network with Tanh activation, and $\boldsymbol{\alpha}$ represents learned attention weights over temporal lags.

D.3. HF Decoder with Spatial Deformation

The HF decoder generates a base spatial pattern and applies a learned spatially-varying deformation to correct for velocity mismatches:

$$\mathbf{u}_{\text{base}}(t) = \gamma \cdot \mathcal{D}_{\text{HF}}(\mathbf{z}_{\text{HF}}(t); \boldsymbol{\theta}_{\text{HF}}) \in \mathbb{R}^n, \quad (20)$$

where γ is a learnable scale parameter initialized to 0.5.

To handle spatially and temporally varying wave velocities, we apply a deformation-based correction:

$$\boldsymbol{\delta}(t) = \tanh(\mathcal{F}_{\text{shift}}(\mathbf{z}_{\text{HF}}; \boldsymbol{\theta}_{\text{shift}})) \cdot \delta_{\text{max}} \in \mathbb{R}^n, \quad (21)$$

$$\mathbf{a}(t) = \frac{1}{2} \text{Softplus}(\mathcal{F}_{\text{amp}}(\mathbf{z}_{\text{HF}}; \boldsymbol{\theta}_{\text{amp}})) + \frac{1}{2} \in \mathbb{R}^n, \quad (22)$$

where $\boldsymbol{\delta}$ is a position-dependent shift field bounded by δ_{max} grid points (typically $\delta_{\text{max}} = 10$), and \mathbf{a} is a positive amplitude modulation field centered around 1.

The final HF output is obtained via spatial warping with periodic boundary conditions:

$$u_{\text{HF}}(x_i) = a_i \cdot u_{\text{base}}((x_i + \delta_i) \bmod L_x), \quad (23)$$

where bilinear interpolation is used for non-integer shifts to ensure smoothness.

E. Training Pipeline Details

This appendix provides complete details of the four-stage training pipeline for the Cheap2Rich model.

E.1. Stage 1: SHRED Training on Simulation

A standard SHRED model is first trained on simulation data with sparse sensor inputs. The model consists of an LSTM that maps sensor histories to a latent space, followed by a decoder MLP:

$$\mathcal{L}_{\text{Stage 1}} = \frac{1}{m} \sum_{k=1}^m \|\mathcal{D}_{\text{LF}}(\mathcal{E}_{\text{LF}}(\mathbf{S}_{t_k-L:t_k})) - \mathbf{u}_k\|_2^2, \quad (24)$$

where \mathcal{E}_{LF} denotes the LSTM encoding and \mathcal{D}_{LF} denotes the decoder. This pretrained SHRED model captures the dominant dynamics of the inexpensive simulation and serves as the LF pathway in the multi-scale architecture.

E.2. Stage 2: Latent GAN Training

The generator \mathcal{G} and discriminator \mathcal{D} are trained to align latent distributions:

$$\min_{\theta_G} \max_{\theta_D} \mathcal{L}_D + \mathcal{L}_G, \quad (25)$$

where latent codes are extracted from both simulation and real sensor data using the frozen LF encoder.

E.3. Stage 3: HF-SHRED Training with Spectral Sparsity

The HF pathway is trained with sensor-only supervision combined with a spectral sparsity regularizer. Let k_c denote a user-specified cutoff frequency. The training objective is:

$$\mathcal{L}_{\text{Stage 3}} = \mathcal{L}_{\text{sensor}} + \lambda \mathcal{R}_{\text{freq}}(\tilde{\mathbf{u}}_{\text{HF}}) + \mu \mathcal{L}_{\text{mag}}, \quad (26)$$

where each term is defined as follows.

Sensor Residual Loss. The HF output must match the observed residual at sensor locations:

$$\mathcal{L}_{\text{sensor}} = \|\mathbf{M}\tilde{\mathbf{u}}_{\text{HF}}(t) - \mathbf{r}_t\|_2^2. \quad (27)$$

Bandlimited Spectral Sparsity. Let $\hat{\mathbf{u}}_{\text{HF}}(k)$ denote the discrete Fourier coefficients of $\tilde{\mathbf{u}}_{\text{HF}}$ obtained via rFFT. The regularizer encourages sparsity within a specified frequency band while penalizing energy in higher frequencies:

$$\mathcal{R}_{\text{freq}}(\tilde{\mathbf{u}}_{\text{HF}}) = \underbrace{\frac{\sum_{k=0}^{k_c} |\hat{u}_{\text{HF}}(k)|}{\sqrt{\sum_{k=0}^{k_c} |\hat{u}_{\text{HF}}(k)|^2 + \epsilon}}}_{\text{sparsity within } k \leq k_c} + \beta \underbrace{\frac{\sum_{k>k_c} |\hat{u}_{\text{HF}}(k)|^2}{\sum_{k \geq 0} |\hat{u}_{\text{HF}}(k)|^2 + \epsilon}}_{\text{high-frequency energy ratio}}, \quad (28)$$

where k_c is a user-specified cutoff frequency and $\beta \gg 1$ (typically $\beta = 100$) penalizes energy above this cutoff to encourage sparse, low-frequency corrections.

For the RDE experiments with $p = 25$ sensors over a domain of $n = 100$ grid points, we set the cutoff frequency to $k_c = 12$, which empirically balances reconstruction fidelity with spectral parsimony.

Magnitude Constraint. To prevent the HF component from dominating:

$$\mathcal{L}_{\text{mag}} = [\max(0, \|\tilde{\mathbf{u}}_{\text{HF}}\|_1 - \tau)]^2, \quad (29)$$

where τ is estimated from the sensor residual scale.

Warmup Schedule. The sparsity weight λ is ramped from 0 to its target value over an initial warmup period to allow the model to first learn the basic residual structure before enforcing sparsity.

E.4. Stage 4: Fine-Tuning

The HF pathway is fine-tuned with reduced sparsity weight $\lambda' = 0.1\lambda$ to allow greater expressivity while maintaining the learned sparse structure.

E.5. Inference and Full-State Reconstruction

At inference time, given a new sensor history $\mathbf{S}'_{t-L:t}$, the full-state estimate is computed as:

$$\mathbf{z}_{\text{LF}} = \mathcal{E}_{\text{LF}}(\mathbf{S}'_{t-L:t}), \quad (30)$$

$$\tilde{\mathbf{z}}_{\text{LF}} = \mathbf{z}_{\text{LF}} + \mathcal{G}(\mathbf{z}_{\text{LF}}), \quad (31)$$

$$\tilde{\mathbf{u}}_{\text{LF}} = \mathcal{P}_{k_c}(\mathcal{D}_{\text{LF}}(\tilde{\mathbf{z}}_{\text{LF}})), \quad (32)$$

$$\mathbf{r}_\ell = \mathbf{s}'_{t-\ell} - \mathbf{M}\tilde{\mathbf{u}}_{\text{LF}}, \quad \ell = 0, \dots, L-1, \quad (33)$$

$$\tilde{\mathbf{u}}_{\text{HF}} = \text{Deform}(\mathcal{D}_{\text{HF}}(\mathcal{E}_{\text{HF}}(\mathbf{R}_{t-L:t}))), \quad (34)$$

$$\tilde{\mathbf{u}}'(t) = \tilde{\mathbf{u}}_{\text{LF}}(t) + \tilde{\mathbf{u}}_{\text{HF}}(t). \quad (35)$$

E.6. Hyperparameter Configuration

Table 4 summarizes the default hyperparameters.

E.7. Computational Cost and Model Complexity

Table 5 summarizes the computational cost and model complexity.

Table 5. Computational cost and model complexity.

Metric	Value
<i>Model Complexity</i>	
LF-SHRED parameters	4.9 K
HF-SHRED parameters	163.9 K
Total parameters	168.8 K
<i>Training Time</i>	
Stage 1 (LF-SHRED)	7.92 sec
Stage 2 (GAN)	1.09 sec
Stage 3 (HF-SHRED + Fine-tuning)	38.87 sec
Total	47.88 sec
<i>Hardware</i>	
CPU	Apple M4 Pro
Memory	24 GB

Table 4. Default hyperparameters for the Sparse-Frequency DA-SHRED architecture.

Component	Parameter	Value
Data	Number of sensors	25
	Temporal lags L	25
	Train/Valid split	80%/20%
LF-SHRED Encoder	Hidden dimension d_z	32
	LSTM layers	2
	Dropout rate	0.1
	Normalization	LayerNorm
LF Decoder	Hidden layers	[128, 128]
	Activation	ReLU
GAN	Generator hidden	64
	Discriminator hidden	64
	Activation	LeakyReLU
HF-SHRED	Hidden dimension	32
	LSTM layers	2
	Dropout rate	0.1
	Lag attention	True
	Attention hidden	64
	Velocity correction	Deformation
HF Decoder	Max spatial shift	± 10 grid points
	Hidden layers	[128, 128]
	Deformation net	[128, N]
	Amplitude net	[64, N]
Sparsity	Scale γ init	0.5
	λ_{sparse}	0.1
	Out-of-band penalty β	100.0
Optimization	Fine-tune λ'_{sparse}	0.01
	Batch size	32
	Optimizer	Adam / AdamW

F. Comparison to other methods

This appendix benchmarks our approach against standard supervised baselines. We assume access to paired low-fidelity and high-fidelity datasets, and consider the reconstruction task

$$\mathbb{R}^p \ni s_t \mapsto u'_t \in \mathbb{R}^n,$$

where s_t denotes the p sensor measurements at time t and u'_t the corresponding high-fidelity state. We compare (i) SHRED models that use a history of sensor measurements (lagged inputs) and (ii) feed-forward MLPs that map sensors to state instantaneously. For each architecture, we evaluate two training strategies: training solely on high-fidelity data, and pretraining on low-fidelity data followed by fine-tuning on high-fidelity data.

All models are evaluated with an RMSE calculated on the final 50 snapshots of the high-fidelity dataset, held out from training, as well as SSIM evaluated at the entire high-fidelity dataset. When pretraining is used, we train on 250 preprocessed snapshots from Koch’s model before fine-tuning on the high-fidelity data.

F.1. SHRED trained on high-fidelity data only

We use $p = 25$ sensors, $L = 5$ lags, and a latent dimension $d_z = 32$. The model is trained for 500 epochs with Adam (initial learning rate 10^{-3}), achieving RMSE = 0.102237 on the test set and SSIM of 0.171135 on train + test. To enable inference

for $t \leq L$, we pad the sensor histories in both the training and test sets with zeros at the initial time steps. Reconstructions are shown in Figure 9.

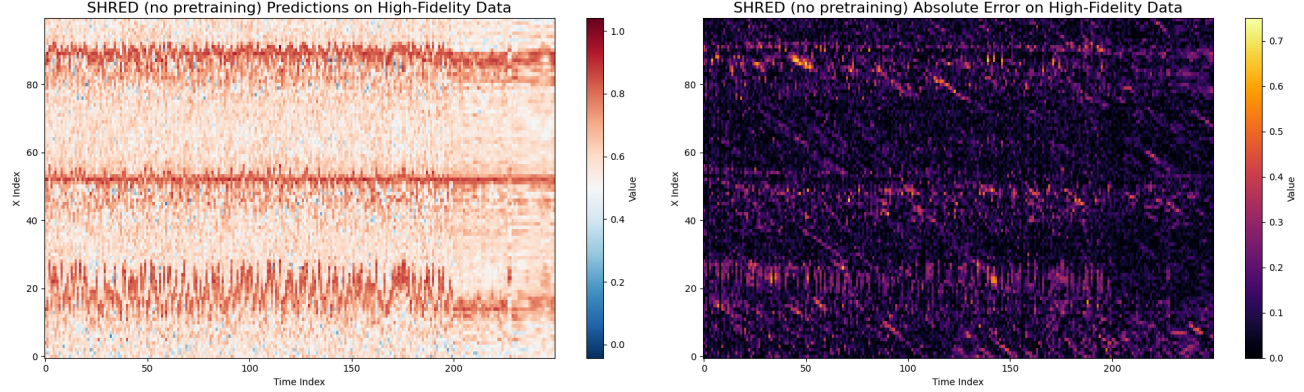


Figure 9. SHRED trained on high-fidelity data only.

F.2. SHRED pretrained on Koch’s model, then fine-tuned on high-fidelity data

We again use $p = 25$, $L = 5$, and $d_z = 32$. The model is pretrained for 500 epochs on Koch’s data and then fine-tuned for 300 epochs on the high-fidelity data using Adam (initial learning rate 10^{-3}). This yields RMSE = 0.107945 on the test set, and SSIM of 0.176757 on train + test. As above, sensor histories are zero-padded to support inference for $t \leq L$. Reconstructions are shown in Figure 10.

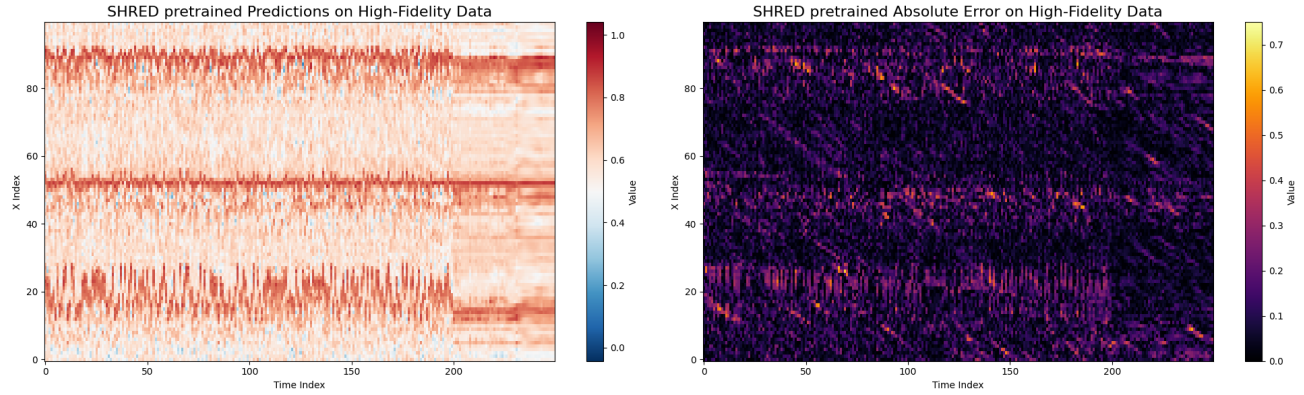


Figure 10. SHRED pretrained on Koch’s data and fine-tuned on high-fidelity data.

F.3. MLP trained on high-fidelity data only

We use $p = 25$ sensors and a feed-forward MLP with layer widths [25, 128, 128, 128, 100] and ReLU activations. The model achieves RMSE = 0.093735 on the test set and SSIM of 0.213414 on train + test. Reconstructions are shown in Figure 11.

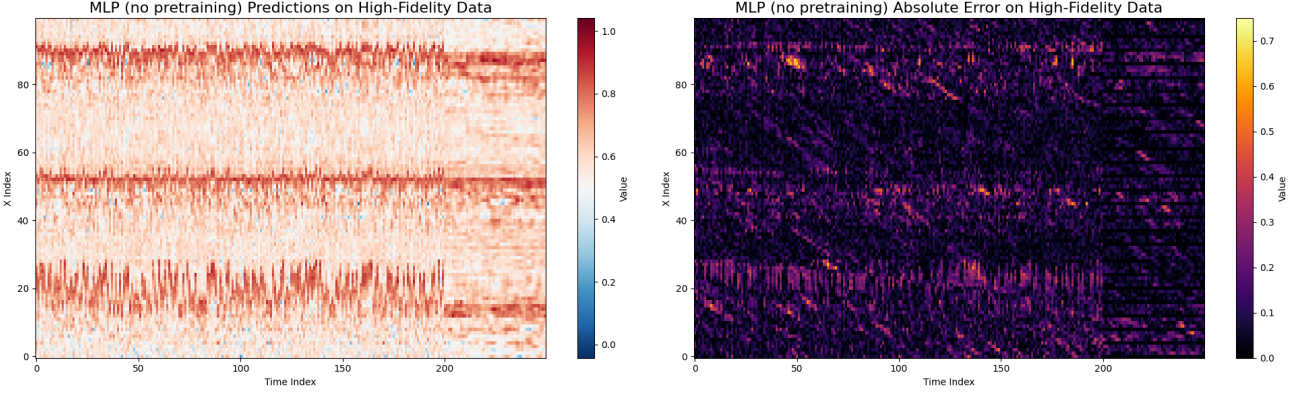


Figure 11. MLP trained on high-fidelity data only.

F.4. MLP pretrained on Koch's model, then fine-tuned on high-fidelity data

We use the same MLP architecture as above. The model is pretrained for 500 epochs on Koch's data and then fine-tuned for 300 epochs on the high-fidelity data with Adam (initial learning rate 10^{-3}), achieving RMSE = 0.107945 on the test set, and SSIM of 0.213414 on train + test. Reconstructions are shown in Figure 12.

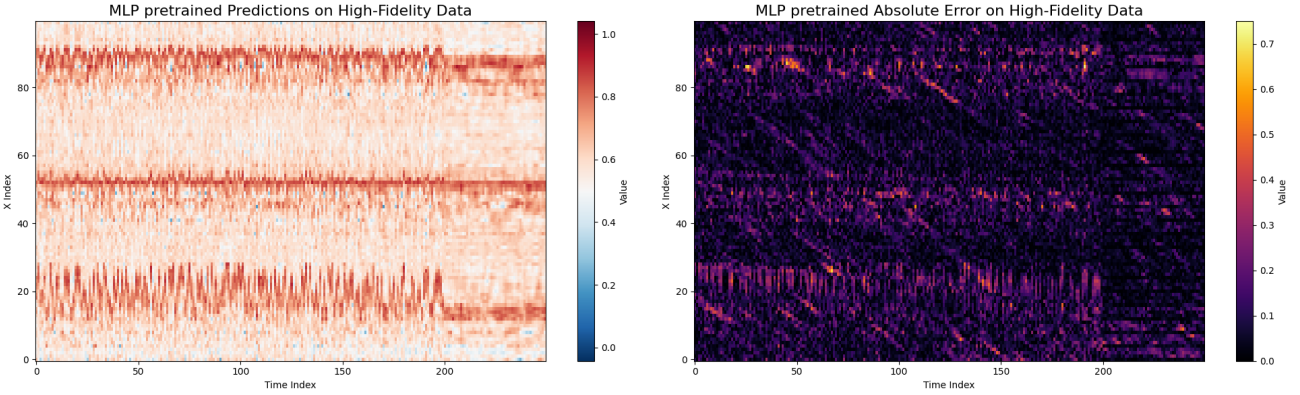


Figure 12. MLP pretrained on Koch's data and fine-tuned on high-fidelity data.

F.5. Cheap2Rich (ours)

Figure 13 reports reconstructions produced by Cheap2Rich. The test-set error is RMSE = 0.1031, and the SSIM on the entire high-fidelity dataset is 0.3638. While the aggregate RMSE is comparable to the baselines, the reconstructions better preserve the salient spatiotemporal structure, which is also explained by the much higher SSIM. In particular, the three dominant wavefronts are sharper and more consistently separated, and fine-scale features are recovered more faithfully, including the colder regions near $(x, t) = (80, 25)$ and $(45, 75)$.

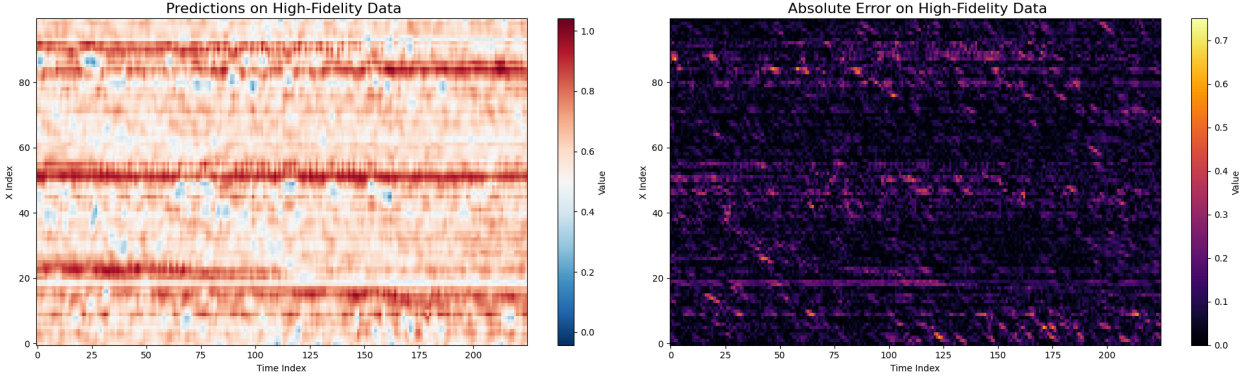


Figure 13. Cheap2Rich reconstructions on the high-fidelity test set.

G. SINDy Framework and Simulation Integration Details

This appendix provides additional details on the SINDy-based physics discovery described in Section 5.

G.1. SINDy Framework for Discrepancy Modeling

Given the LF reconstruction $\tilde{\mathbf{u}}_{\text{LF}}$, the HF correction $\tilde{\mathbf{u}}_{\text{HF}}$, and the known Koch's simulation \mathbf{u}_{sim} , we can pose three complementary discovery problems:

LF Correction Dynamics. The GAN-based latent alignment induces a correction to the simulation output. We seek to identify the functional form of this correction:

$$\frac{\partial}{\partial t} (\tilde{\mathbf{u}}_{\text{LF}} - \mathbf{u}_{\text{sim}}) = f(\Delta u, \Delta u_x, u_{\text{LF}}, u_{\text{LF},x}, \dots), \quad (36)$$

where $\Delta u = \tilde{\mathbf{u}}_{\text{LF}} - \mathbf{u}_{\text{sim}}$ denotes the LF correction field.

HF Component Dynamics. The high-frequency pathway captures fine-scale physics absent from the Koch's model. We identify its governing dynamics:

$$\frac{\partial \tilde{\mathbf{u}}_{\text{HF}}}{\partial t} = g(u_{\text{HF}}, u_{\text{HF},x}, u_{\text{LF}}, u_{\text{LF}} \cdot u_{\text{HF}}, \dots). \quad (37)$$

Direct Missing Physics. Most directly, we can identify the total discrepancy between real and simulated dynamics:

$$\frac{\partial}{\partial t} (\mathbf{u}_{\text{real}} - \mathbf{u}_{\text{sim}}) = h(u, u_x, u_{xx}, u \cdot u_x, \dots). \quad (38)$$

where u denotes \mathbf{u}_{sim} .

G.2. Library Construction and Sparse Regression

For each discovery problem, we construct a library of candidate nonlinear terms Θ and solve the sparse regression problem:

$$\frac{\partial \mathbf{u}}{\partial t} = \Theta(\mathbf{u}, \mathbf{u}_x, \mathbf{u}_{xx}, \dots) \xi, \quad (39)$$

where ξ is a sparse coefficient vector recovered via sequential thresholded least squares (STLSQ) (Brunton et al., 2016).

The candidate library is tailored to the physical context of RDE dynamics. For the direct missing physics discovery, we use:

$$\Theta = [1, u, u^2, u^3, u_x, u_{xx}, u \cdot u_x, \Delta u, \Delta u_x, \dots], \quad (40)$$

where spatial derivatives are computed spectrally via FFT to ensure accuracy (Brunton & Kutz, 2022). The library is normalized column-wise before regression to ensure fair coefficient comparison across terms of different magnitudes.

The STLSQ algorithm iteratively performs least-squares regression and thresholds small coefficients to zero, promoting sparsity while maintaining accuracy. We employ adaptive thresholding, starting from $\alpha = 0.001$ and incrementing until the discovered equation contains 2–8 active terms, balancing parsimony with expressiveness.

G.3. Simulation Integration

The discovered equations provide two pathways for improving the Koch’s model without requiring the neural network at inference time.

Direct Correction. The most straightforward approach uses the discovered missing physics equation directly. The modified governing equation becomes:

$$\frac{\partial u}{\partial t} = [\text{Koch's terms}] + \gamma \cdot h(u, u_x), \quad (41)$$

where $h(u, u_x) = 0.72 - 3.79u + 6.24u^2 - 3.33u^3 + 0.40u_x - 0.40u \cdot u_x$ is the discovered correction functional and γ is a tunable scale factor that accounts for normalization differences between training data and simulation variables.

Hierarchical Correction. Alternatively, the LF and HF corrections can be applied separately, enabling independent tuning of large-scale adjustments versus fine-scale dynamics:

$$\frac{\partial u}{\partial t} = [\text{Koch's terms}] + \gamma_{\text{LF}} \cdot f(\Delta u, u) + \gamma_{\text{HF}} \cdot g(u_{\text{HF}}, u_{\text{LF}}), \quad (42)$$

where f and g are the discovered LF correction and HF dynamics, respectively. This approach provides finer control but requires tracking both components during simulation.

G.4. Connection to DA-SHRED Framework

The SINDy-based discovery presented here extends the methodology of (Bao & Kutz, 2025) to the multi-scale setting. While the original DA-SHRED framework demonstrated discrepancy modeling for systems with a single learned correction, the multi-scale architecture provides a natural decomposition that yields richer physical insight:

- The **LF correction** captures what the latent-space GAN alignment contributes—primarily amplitude and baseline adjustments that align the simulation manifold with reality.
- The **HF dynamics** reveal the structure of physics entirely absent from the simplified model, including the coupling between fine-scale fluctuations and the dominant wave structure.
- The **direct missing physics** provides a single equation summarizing all corrections needed, suitable for integration into simulations where the model discrepancy is perturbative—i.e., when the simulation is not far from reality.

This combined discovery approach—enabled by the Cheap2Rich architecture—provides both interpretability and actionable model corrections, advancing beyond pure reconstruction toward genuine physics discovery.